

Update of the Seismogenic Potential of the Upper Rhine Graben Southern Region

Sylvain Michel^{1,2}, Clara Duverger², Laurent Bollinger², Jorge Jara¹, Romain Jolivet^{1,3}

¹Laboratoire de Géologie, Département de Géosciences, Ecole Normale Supérieure, PSL Université, CNRS UMR 8538, 24 Rue Lhomond, 75005, Paris, France.

²CEA, DAM, DIF, F-91297 Arpaçon, France

³Institut Universitaire de France, 1 rue Descartes, 75005, Paris

Correspondence to: Sylvain Michel (sylvain_michel@live.fr)

Abstract.

The Upper Rhine Graben (URG), located in France and Germany, is bordered by north-south trending faults, some of which are considered active, posing a potential threat to the dense population and infrastructures on the Alsace plain. The largest historical earthquake in the region was the $M_{6.5\pm 0.5}$ Basel earthquake in 1356. Current seismicity ($M > 2.5$ since 1960) is mostly diffuse and located within the graben. We build upon previous seismic hazard studies of the URG by exploring uncertainties in greater detail and revisiting a number of assumptions. We first take into account the limited evidence of neotectonic activity, then explore tectonic scenarios that have not been taken into account previously, exploring uncertainties for M_{max} , its recurrence time, the b -value, and the moment released aseismically or through aftershocks. Uncertainties on faults' moment deficit rates, on the observed seismic events' magnitude-frequency distribution, and on the moment-area scaling law of earthquakes are also explored. Assuming a purely dip-slip / normal faulting mechanism associated to a simplified 3 main fault model, M_{max} maximum probability is estimated at $M_w 6.1$. Considering this scenario, there would be a 99% probability that M_{max} is less than 7.3. In contrast, with a strike slip assumption associated to a 4 main fault model, consistent with recent paleoseismological studies and the present-day stress field, M_{max} is estimated at $M_w 6.8$. Based on this scenario, there would be a 99% probability that M_{max} is less than 7.6.

28 1 INTRODUCTION

29 The Upper Rhine Graben (URG), located in France and Germany, is bounded by north-south trending faults, some
30 of which are considered active, posing a potential threat to the dense population and the industrial and
31 communication infrastructures of the Alsace plain (Figure 1). The largest historical earthquake in the region was
32 the 1356 Basel earthquake with a maximum intensity equal to or greater than IX (Mayer-Rosa and Cadiot, 1979;
33 Fähr et al., 2009), an earthquake presently associated to a magnitude between $M_{6.5\pm 0.5}$ (Manchuel et al., 2017)
34 and $M_{6.9\pm 0.2}$ (Fähr et al., 2009). Current seismicity ($M > 2.5$ since 1960) is mostly diffuse and located within the
35 graben (Dobre et al., 2022), hence the difficulty to attribute individual events to a given fault segment. The
36 bordering faults themselves are relatively quiet except for the south-eastern section of the graben, near Mulhouse-
37 Basel, where natural seismic sequences (Rouland et al., 1983; Bonjer, 1997) and induced seismicity (Kraft and
38 Deichmann, 2014) have been observed. Seismic activity actually varies along the URG with an increasing rate of
39 events towards the south (Barth et al., 2015). The relative rate between small and large events (b-value from the
40 Gutenberg-Richter law) also increases towards the south indicating a surplus of small earthquakes or a deficit of
41 large events roughly south of Strasbourg (Barth et al., 2015). Focal mechanisms of earthquakes suggest that the
42 region is subject to strike-slip regime with some normal component (Mazzotti et al., 2021), consistent with the
43 large wavelength strain inferred from geodetic data (Henrion et al., 2020). Characterizing the slip rates of the
44 graben's faults based on geodetic data remains challenging. Indeed regional glacial isostatic adjustments, local
45 subsidence and low tectonic strain rates result in a heterogeneous velocity field with values below 0.2 mm/yr and
46 often within measurement uncertainties (Fuhrmann et al., 2015; Henrion et al., 2020).

47 The seismic hazard of the URG has been evaluated by multiple studies at the national/European scale (Grünthal et
48 al., 2018; Drouet et al., 2020; Danciu et al., 2021). Furthermore, the seismic hazard of the southern region of the
49 URG in particular has recently been assessed by Chartier et al. (2017) with a focus on the Fessenheim nuclear
50 power plant (Figure 1). This study evaluates the seismic hazard using a fault-based approach, taking into account
51 the network of potentially active faults characterized by Jomard et al. (2017). This fault-based work involves a
52 moment budget approach, which involves comparing the rate of moment release by seismicity and the rate of
53 moment deficit (MDR) accumulating along locked portions of faults between large earthquakes (i.e. the tectonic
54 loading rate of each fault). Since the period of seismological observation (a few centuries) is too short to be
55 representative of the long-term behavior of seismicity, Chartier et al. (2017) built instead a seismicity model
56 assumed to be representative of the long-term Magnitude-Frequency Distribution (MFD) of earthquakes, a method
57 similarly used in former studies (e.g. Molnar, 1979; Anderson and Luco, 1983; Avouac, 2015). Earthquakes below

58 M_w 5 are disregarded (Bommer and Crowley, 2017; Chartier et al., 2017). Earthquakes between M_w 5 and 6 are
59 assumed to follow the MFD of the catalog of earthquakes they consider. This catalog integrates several sources of
60 instrumental and historical earthquakes including sources from the *Laboratoire de Détection et de Géophysique*
61 of the *Commissariat à l'Énergie Atomique et aux énergies alternatives* (CEA-LDG; <http://www-dase.cea.fr/>) and
62 from the FPEC (French Parametric Earthquake Catalogue; Baumont and Scotti, 2011), the IRSN contribution to
63 SHEEC (SHARE European Earthquake Catalogue; Stucchi et al., 2013). MFDs are estimated based on a French
64 seismotectonic zoning scheme defined by Baize et al. (2013). Earthquakes with magnitude above M_w 6 are assumed
65 to occur on the fault planes (Jomard et al., 2017). Chartier et al. (2017) consider two types of model: (1) Each fault
66 ruptures only as its maximum magnitude event, which is controlled by the surface area of the seismogenic fault
67 segment (characteristic earthquake model); (2) Events follow the Gutenberg-Richter (GR) law with a b-value equal
68 to 1, and the maximum magnitude, M_{max} , is fixed as in the previous model. The recurrence times of the $M_w > 6$
69 events are then calibrated so that the rate of moment released by the seismicity models matches the MDR estimated
70 from neotectonic data (Chartier et al., 2017; Jomard et al., 2017). The authors explore different fault geometries
71 (e.g. dip and seismogenic depth) using a logic-tree methodology and then proceed to the Probabilistic Seismic
72 Hazard Assessment (PSHA) of the region, providing a map of the probability of exceedance of Peak Ground
73 Acceleration (PGA) within a time period.

74 A number of strong assumptions are made within this framework. As mentioned previously, a simplified fault
75 network is used (Jomard et al., 2017), which constrains the seismogenic area available for ruptures. Expert choices
76 have also been made to distribute slip rates (i.e. loading rates) originally attributed to faults that have been removed
77 from the initial fault network (Nivière et al., 2008) on other fault segments. On a number of faults, no estimates of
78 neotectonic slip rate are available (e.g. West Rhenish Fault) and the authors have chosen to apply slip rates
79 equivalent to those from other nearby faults (0.01 to 0.05 mm/yr). The neotectonic data are actually only along-
80 dip slip rate estimates. No along-strike slip rates have yet been published due to the lack of markers to quantify
81 horizontal offsets along faults and this component has thus been ignored. In addition, Chartier et al. (2017) do not
82 consider continuous probabilities as they apply a logic-tree method. Chartier et al (2017) fix the b-value to 1,
83 choose the seismogenic depth to be either 15 or 20 km and do not take into account multi-segment ruptures when
84 estimating a M_{max} for each fault segment.

85 In this study, we build upon Chartier et al. (2017) seismic hazard evaluation of the southern URG by exploring
86 uncertainties in greater detail, revisiting a number of assumptions. We use the methodology from Rollins and

87 Avouac (2019) and Michel et al. (2021), which allows to evaluate the seismogenic potential of faults in a
88 probabilistic fashion and explore uncertainties for parameters such as the b-value or M_{max} . We use the fault
89 network and slip rates taken into account by Nivière et al. (2008), disregarding the Western Rhenish Fault for
90 which, to our knowledge, no slip rate data is available. We assume faults can rupture simultaneously (i.e. multi-
91 segment rupture). In the following sections, we start by describing the concepts and methods we use to constrain
92 the seismogenic potential of the URG, and then describe the data available before discussing the robustness of our
93 results.

94 **2 METHOD**

95 We use the methodology from Michel et al. (2021) in order to estimate the seismogenic potential of the upper
96 Rhine Graben, including M_{max} and its recurrence time. As in Chartier et al. (2017), we produce seismicity models
97 representative of the long-term behavior of earthquakes. We assume that the MFDs of background earthquakes
98 follow a Gutenberg-Richter power law up to M_{max} . We define background earthquakes as mainshocks, as opposed
99 to their subsequent aftershocks. We assume that their timing of occurrence is random, following a Poisson process.
100 Each model is controlled by three parameters: (1) M_{max} , (2) the recurrence time of events of a certain
101 magnitude, τ_c , and (3) the b-value. We use two types of model, namely the tapered and truncated models (Rollins
102 and Avouac, 2019; Michel et al., 2021; Figure S1). The tapered model type assumes a non-cumulative power-law
103 MFD truncated at M_{max} , which gives rise to a tapered MFD in the cumulative form (i.e. the traditional display
104 when representing the Gutenberg-Richter law). The truncated model type assumes instead a MFD with a
105 distribution truncated at M_{max} in the cumulative form.

106 The seismicity models are then tested against three constraints: (1) the moment budget, as in Chartier et al. (2017),
107 which implies that moment released by slip on the fault should match the moment deficit accumulating between
108 earthquakes over a long period of time; (2) the moment-area scaling law, an empirical scaling law relating rupture
109 area to slip for each earthquake, and (3) the MFD of observed seismicity. Each of these constraints are described
110 in more detail in the following sub-sections. The data and associated uncertainties used for the constraints are
111 discussed in the following section (i.e. Section 3).

112 **2.1 Moment budget**

113 A moment budget consists in comparing the rate of moment released from slip events (seismic or aseismic),
114 \dot{m}_0^{Total} , with the moment deficit rate, \dot{m}_0^{def} , accumulating between slip events. The moment deficit rate is defined

115 by the equation $\dot{m}_0^{def} = \int \mu \dot{D}^{def} dA$, where μ is the shear modulus, A is the area that remains locked during the
116 interseismic period (i.e. the potential seismogenic zone), and \dot{D}^{def} is the rate at which slip deficit builds up. Since
117 the distribution of locked segments of faults and their associated loading rates cannot yet be determined for the
118 URG from geodetic measurements, A is assumed to be homogeneous along-strike for each fault, while we consider
119 possible the seismogenic width to change from one fault to another. The rate at which slip deficit builds up, \dot{D}^{def} ,
120 is evaluated based on neotectonic information (see Section 3.1). The total moment released, \dot{m}_0^{Total} is calculated
121 based on the rate of moment release of the long-term seismicity model. Since the long-term seismicity model only
122 considers mainshocks, we included a fourth parameter, α_s , that represents the proportion of moment released by
123 background seismicity (Avouac, 2015), \dot{m}_0^{Bckgrd} , relative to the total moment released (including aftershocks and
124 aseismic afterslip). If $\dot{m}_0^{def} = \dot{m}_0^{Total} = \dot{m}_0^{Bckgrd} / \alpha_s$, then the moment budget is said to be balanced.

125 The cumulative MFD for tapered and truncated seismicity models achieving a balanced moment budget have an
126 analytical form and are a function of M_{max} , b , \dot{m}_0^{def} and α_s (see Rollins and Avouac, 2019, and references therein).
127 We can therefore estimate the probability of a seismicity model balancing the moment budget, P_{Budget} , by
128 sampling the *a priori* distributions of those parameters.

129 **2.2 Moment-area scaling law**

130 According to global earthquake statistics, the moment released by an earthquake, m_0^{Seis} , is proportional to the area
131 of its rupture, A_{eq} , such that $m_0^{Seis} \propto A_{eq}^{3/2}$ (Wells and Coppersmith, 1994; Leonard, 2010; Stirling et al., 2013).
132 We use this scaling to evaluate whether a seismic event of a given magnitude has a rupture area that fits within the
133 seismogenic zone. By considering the spread of the empirical distribution of magnitude vs. area, we assume the
134 probability distribution function of an event of magnitude M_w to be probable considering this scaling, $P_{scaling}$. We
135 use here the self-consistent scaling law, and related uncertainties, as defined by Leonard (2010) in the dip-slip
136 equation (the strike-slip equation is in any case almost the same).

137 **2.3 Earthquake catalog**

138 We test whether the observed MFD from earthquake catalogs may be a sample of the distribution of the long-term
139 seismicity models we are building. Effectively, we evaluate the likelihood of our observed MFD given the
140 distribution of the models. Since we only consider mainshocks, we define the likelihood of the observed seismicity

141 catalog, P_{Cat} , as $P_{Cat} = \prod_i P_{poisson}^{M_i}$, where $P_{poisson}^{M_i}$ is the probability to observe $n_{obs}^{M_i}$ events, within the magnitude
 142 bin M_i , occurring during the time period $t_{obs}^{M_i}$, assuming the long-term mean recurrence of events is $\tau_{model}^{M_i}$:

$$143 P_{poisson}^{M_i}(n_{obs}^{M_i}, t_{obs}^{M_i}, \tau_{model}^{M_i}) = \frac{(t_{obs}^{M_i}/\tau_{model}^{M_i})^{n_{obs}^{M_i}}}{(n_{obs}^{M_i})!} e^{-t_{obs}^{M_i}/\tau_{model}^{M_i}}.$$

144 Effectively, for a given seismicity model, we generate randomly 2500 declustered earthquake catalogs. We
 145 evaluate the likelihood of each catalog and define P_{Cat} as the average of these likelihood values.

146 Note that we follow the recommendation by Felzer (2008) while exploring magnitude uncertainties and correct
 147 the magnitudes of each event by $\Delta M = (b^2 \sigma^2)/(2 \log_{10}(e))$, where b is the declustered catalog b -value, σ is the
 148 standard deviation for the event's magnitude, and e is the exponential constant.

149 2.4 Seismicity model probability and marginal probabilities

150 Finally, the probability of a seismicity model is defined as $P_{SM} = P_{Budget} P_{Cat} P_{scaling}$ which depends, among
 151 others, on M_{max} and b (Michel et al., 2021). The evaluation of the parameters to estimate P_{SM} are discussed in
 152 Section 3. Marginal probabilities such as $P_{M_{max}}$, the probability of M_{max} , and P_b , the probability of the b -value,
 153 can be estimated based on P_{SM} . We also define $P(\tau_{max} | M_{max})$ as the probability of the rate of M_{max} , and
 154 $P(\tau | M_w)$ as the probability of the rate of events with magnitude M_w , which accounts for all earthquakes from all
 155 of the models (i.e. not only M_{max}). Probabilities needed for estimating seismic hazard (e.g. PSHA) such as the
 156 probability to have an event above magnitude M_w for a time period T , $P(M > M_w | T)$, can likewise be evaluated.

157 3 DATA AND ASSOCIATED UNCERTAINTIES

158 We present in this section the data and their associated uncertainties used to evaluate each constraint. Hereafter,
 159 the \mathcal{U} and \mathcal{N} symbols will stand for uniform and normal distribution, respectively. Table 1 summarizes the
 160 uncertainties taken for each parameter.

161 3.1 Neotectonic data, seismogenic along-dip width and moment deficit rate

162 In order to evaluate the MDR for the moment budget constraint (Section 2.1), we must infer estimates of loading
 163 rate (i.e. \dot{D}^{def}) for each fault taken into account. The slip rate on each fault is taken from Nivière et al. (2008) for
 164 the Rhine River, Black Forest, Weinstetten and Lehen-Schonberg faults (the Landeck or West Renish faults are
 165 not considered). Their slip rates rely on estimates of the cumulative vertical displacement of the faults based on

166 Pliocene-Quaternary sediments thickness variations measured from 451 boreholes, assuming that the
167 accommodation space opened by tectonic motion is completely balanced (or over-balanced) by sedimentation.
168 However, potential erosional periods due to the piracy of the Rhine River might bias the measurements, thus the
169 values are to be interpreted as maximum displacement estimates. Nivière et al. (2008) inferred vertical slip rates
170 of 0.07 and 0.17 mm/yr from the age of the sediments for the Rhine River and Weinstetten faults respectively. The
171 Lehen-Schonberg fault slip rate reaches between 0.04 and 0.1 mm/yr. While borehole observations do not allow
172 to conclude on the Pliocene-Quaternary slip rate of the Black Forest fault, this structure is suggested to be inactive
173 during this time period, and that the deformation is now accommodated by the other aforementioned faults (Nivière
174 et al., 2008). Note that these are vertical slip rate estimates and the along-strike component is for the moment
175 neglected. For the moment rate calculation, we project vertical slip rates on the along-dip direction considering
176 the dip angles of each fault.

177 The seismogenic down-dip extent of a fault depends on the temperature gradient (e.g. Oleskevich et al., 1999),
178 among other parameters. Indeed, between the isotherms 350°C and 450°C, quartzo-feldspathic rocks undergo a
179 transition in frictional properties (Blanpied et al., 1995) from a rate-weakening (<350°C), potentially seismogenic
180 behavior to a rate-strengthening (>450°C), stable sliding behavior (Dieterich, 1979; Ruina, 1983). The geothermal
181 gradient below the URG is higher than in the surrounding regions due to its tectonic history (Freyark et al.,
182 2017). Based on borehole temperature measurements from Guillou-Frottier et al. (2013), we estimate the envelopes
183 of the geothermal gradient in the southern URG (Figure S2), assuming a linear temperature gradient with depth,
184 and show that the frictional property transition would occur between depths of 6 (shallowest position of the 350°C
185 isotherm; Figure S2) and 18 km (deepest position of the 450°C isotherm; Figure S2). In this study, we define the
186 PDF of the seismogenic down-dip extent as a uniform distribution between 0 and 6 km depth associated with a
187 linear taper down to 18 km. The linearity of the taper implies that the position of the fault's transition to a fully
188 rate-strengthening behavior (>350-450°C) has a uniform probability to fall between 6 km (shallowest position of
189 the 350°C isotherm according to Figure S2) and 18 km depth (deepest position of the 450°C isotherm; Figure S2),
190 i.e. *Rate-Strengthening Transition* $\in \mathcal{U}(6,18)$ km.

191 Additionally, the southern part of the URG is the site of a potash-salt evaporitic basin (Lutz and Cleintuar, 1999;
192 Hinsken et al., 2007; Freyark et al., 2017), which reaches a maximum depth of ~2 km. Such formations may not
193 accumulate any moment deficit as the yield stress of evaporites is very low (Carter and Hansen, 1983). We assume
194 each fault is potentially impacted by this formation, hence modulating the seismogenic thickness and in turn the

195 seismogenic area available for a rupture. The resulting PDF for the seismogenic thickness is the convolution of
196 the PDF of the down-dip extent of the seismogenic zone with the PDF of the evaporitic basin thickness taken as
197 $U(0,2)$ km.. Combining both temperature and salt basin assumptions leads to a PDF of the along-dip seismogenic
198 width, which is uniform down to ~ 5 km and decreases linearly until ~ 17 km (Figures S3 to S6).

199 The moment deficit is then the product of the length of each fault, their seismogenic width, the neo-tectonic long-
200 term slip rate, and the shear modulus that we fix to 30 GPa (same as in Chartier et al., 2017). Each fault is assumed
201 to have its own seismogenic width. The moment deficit rate of each fault is shown in Figure 1. The PDFs for each
202 of the fault's constitutive parameters are shown in Figure S3 to S6. By considering the range of the fault's
203 geometrical parameters, which considers also the Black Forest Fault even though it is assumed to be non-active,
204 we obtain the moment-area constraint shown in Figure 2. Events up to $M_w 6.5$ are equiprobable while those
205 above $M_w 7.7$ are extremely improbable.

206 3.2 Instrumental and historical seismicity catalogs

207 To constrain the MFD of the long-term seismicity models with an observational seismicity catalog, as described
208 in Section 2.3, we need to evaluate from the observational catalog the number of events per magnitude bin $n_{obs}^{M_i}$
209 over a period of time $t_{obs}^{M_i}$ (Section 2.3). We use the earthquake catalog from Drouet et al. (2020). This catalog was
210 built from multiple former catalogs. It relies mostly on the FCAT-17 catalog (Manchuel et al., 2018), which is
211 itself a combination of the instrumental catalog SiHex (SIsmicit  de l'HEXagone; Cara et al., 2015) for the 1965-
212 2009 period, and a historical catalog based on the macroseismic database of SISFRANCE (BRGM, IRSN, EDF),
213 intensity prediction equations from Baumont et al. (2018) and the macroseismic moment magnitude determination
214 from Traversa et al. (2018) for the 463-1965 period. Events located more than 20 km from the French border, not
215 provided by the FCAT-17, are based on the SHEEC catalog (Stucchi et al., 2013; Woessner et al., 2015). Finally,
216 events between 2010 and 2016 come from the CEA-LDG bulletins (<https://www-dase.cea.fr>). All event
217 magnitudes are given in M_w and uncertainties are provided. Anthropogenic events are expected to be already removed
218 from the catalog (Cara et al., 2015; Manchuel et al., 2018).

219 We select events within the coordinates $[6^\circ, 8.5^\circ]$ longitude and $[47^\circ, 49.5^\circ]$ latitude, i.e. a broad region covering
220 the whole URG, and divide the catalog into two time periods, an instrumental period and a historical one taking
221 events from 1980 onwards and 1850 onwards, respectively. We decluster both catalogs to compare them with the
222 long-term seismicity models (Section 2.3). Declustering is based on the methodology of Marsan et al. (2017),
223 which evaluates the probability that an earthquake is a mainshock. Declustering is applied based on a completeness

224 magnitude, M_c , of 2.2 and 3.2 for the instrumental and historical catalogs, respectively (Text S1; Figures S7 and
 225 S8). From the resulting catalogs, we keep events from 1994 onwards and 1860 onwards for the instrumental and
 226 historical catalogs, respectively (Figures S7 and S8), in order to avoid border effects from declustering. For the
 227 instrumental catalog, 1994 is also the date from which the seismicity rate appears relatively constant (Figure S7).
 228 We then select events in the region of interest (i.e. the southern part of the URG), taking into account only
 229 earthquakes located within a 10 km buffer around the faults considered, including the Black Forest fault (Figure
 230 3). Note that since no events below M_c are considered, there is a lack of events which falls in the magnitude bins
 231 directly above M_c while exploring magnitude uncertainties. Thus, when applying the earthquake catalog constraint
 232 (Section 2.3), we take events with $M_w \geq 2.8$ and $M_w \geq 4.3$ for the instrumental and historical catalogs,
 233 respectively (Felzer, 2008) (Figure 3).

234 **3.3 Constitutive parameters of seismicity models**

235 As mentioned in Section 2.1, the cumulative MFD for tapered and truncated seismicity models balancing the
 236 moment budget can be defined as a function of M_{max} , b , \dot{m}_0^{def} and α_s . We explore these parameters using a grid
 237 search with M_{max} and b sampled uniformly over $M_{max} \in \mathcal{U}(4.5, 9.9)$ and $b \in \mathcal{U}(0.1, 1.45)$, respectively. Based
 238 on global statistics of the post-seismic response following earthquakes (Alwahedi and Hawthorne, 2019; Churchill
 239 et al., 2022), we assume that the PDF of α_s is a Gaussian distribution with $\mathcal{N}(0.9, 0.25)$ (Figure S9). Finally, the
 240 PDF of the MDR for each fault is assumed to be uniform between 0 and the estimate based on the maximum slip
 241 rate from Nivière et al. (2008) (Section 3.1). We thus include scenarios for which almost no moment deficit
 242 accumulates on the fault (i.e. the fault slips aseismically or accumulates no strain over long periods of time). This
 243 assumption contrasts with the choice made by Chartier et al. (2017) who assume that each fault is fully locked
 244 over a seismogenic width terminating at either 15 or 20 km. Doing so, we explore a broad range of possible models.

245 **4 RESULTS**

246 The combination of constraints (Section 2) leads to the results shown in Figure 4. For the truncated model, the
 247 marginal probability of P_{SM} in the M_{max} and τ_{max} space is represented by the gray shaded distribution in Figure
 248 4 (not shown for the tapered model since the models taper at M_{max}). The marginal probability of M_{max} for the
 249 tapered model (in green) peaks at 6.1, while the one for the truncated model (in blue) is bi-modal with peaks at 5.2
 250 and 5.8. For the truncated model (not the tapered model for the same reason as previously indicated), the marginal
 251 probability $P(\tau_{max} | M_{max} = 5.8)$ (solid blue line in the y-axis) peaks at ~ 1000 yrs. Taking $M_{max} = 6.6$ or 7.0, a

252 number close to the estimated magnitude of the 1356 Basel earthquake, the marginal probability would instead
253 peak at $\sim 16,000$ and $\sim 80,000$ yrs, respectively.

254 The marginal probabilities $P(\tau | M_w = 6.1)$ and $P(\tau | M_w = 5.8)$ for the tapered and truncated models (green and
255 blue dotted lines on the y-axis, respectively), which take all events from the seismicity models into account (not
256 only M_{max}), have instead peaks at $\sim 16,000$ yrs and $\sim 10,000$ yrs, respectively. The marginal probability P_b peaks
257 at ~ 0.85 and 0.9 for the tapered and truncated models, respectively.

258 The effect with and without the moment-area scaling law is shown in Figure 5. Adding the scaling law constraint
259 does not change the mode of $P_{M_{max}}$ but completely rejects scenarios with $M_{max} > 7.8$.

260 Finally, the probabilities $P(M > M_w | T)$ for $T = 100$ and $10,000$ yrs are also shown in Figure 5. As an example,
261 the probability of occurrence for an event above $M_w 6.5$ (similar to the 1356 Basel earthquake) for an observational
262 period of 100 yrs is $\sim 0.1\%$ for both the tapered and truncated models. For an event above $M_w 6.0$ and for the same
263 period, this probability is instead $\sim 1\%$ for both models (see zoom in Figure 5.c).

264 The correlations between M_{max} , the moment deficit rate, the b -value, and α_s , for both the tapered and truncated
265 models but without the scaling law constraint, are shown in Figures S10 and S11. For both models, probable M_{max}
266 increases with increasing b -value (Figure S10.a and S11.a), highlighting strong interdependency between the two
267 parameters. Raising the moment deficit rate will control the minimum probable M_{max} (Figures S10.b and S11.b)
268 but will also tend to exclude scenarios with a high b -value (> 1.25 ; Figures S10.f and S11.f). While other trends
269 are expected between parameters, they seem less visible likely due to the uncertainties of the parameters explored,
270 and we thus do not pursue further analysis between those parameters.

271 The results if we combine the PDFs from the tapered and truncated models using a mixture distribution are shown
272 in Figure S12. $P_{M_{max}}$ has a main peak at 5.9 and a smaller peak at 5.2 , which originates from the truncated model.
273 $P(\tau | M_w = 5.9)$ peaks instead at $\sim 13,000$ yrs.

274 **5 DISCUSSION**

275 **5.1 Sensibility to earthquake catalog declustering**

276 The catalog declustering (i.e. removal of aftershocks) may have a significant impact on the results (Section 2.3),
277 influencing the shape of the observed MFD of earthquakes. In this study, we applied the methodology of Marsan

278 et al. (2017), which is based on the ETAS framework and intrinsically assumes that background events have
279 Poisson behavior. Other declustering methodologies are available and we test here the one from Zaliapin and Ben-
280 Zion (2013) based on the nearest-neighbor distances of events in the space-time-energy domain. The results from
281 this methodology produce background seismicity catalogs with more events than the one from Marsan et al. (2017)
282 (Text S2 and Figures S13 to S15), but infers larger b-values when combining the instrumental catalog with the
283 historical one (as inferred by Figure 6.b). The analysis of the seismogenic potential of the URG using Zaliapin and
284 Ben-Zion (2013) methodology results with $P_{M_{max}}$ peaking at M6.3 for the tapered model, and is still bi-modal for
285 the truncated model, with peaks at M5.2 and M5.9 (Figure 6). Unlike with Marsan et al. (2017), the peak at lower
286 magnitude for the truncated model is more probable than the one at larger magnitude. The most probable M_{max}
287 for both models are slightly shifted to lower magnitudes than the values estimated using Marsan et al. (2017)
288 methodology, but the width of the PDFs appears unchanged to first order. The resulting marginal probabilities
289 $P(\tau | M_w = 5.9)$ and $P(\tau | M_w = 5.8)$ for the tapered and truncated models both peak at ~8,000 yrs.

290 **5.2 Source of seismicity**

291 We initially selected earthquakes within a 10 km buffer zone around the faults to reflect the spatial strain pattern
292 of a vertical fault blocked down to a depth of 10 km. Nevertheless, the locking depth could potentially be deeper,
293 down to ~18 km as suggested in Section 3.1. In this respect, we also provide results if events are selected within
294 20 km of the faults (Figures S16 and S17). Under these conditions, the seismicity rates of the observational
295 earthquake catalogs are higher and constrain the long-term seismicity models to cases that produce higher moment
296 release rate. $P_{M_{max}}$ thus favours events with a lower magnitude than the one using events within 10 km (Figure 5;
297 Section 4). The tapered model peaks at M_w 5.9, instead of 6.1, while the truncated model peaks twice at M_w 5.2
298 and 5.8, in a similar manner to the reference scenario in Section 4, except that the peak at M_w 5.2 is now the most
299 probable.

300 However, current seismicity in the URG is seemingly diffuse and it is difficult to associate it with a fault in
301 particular (Dobre et al., 2022). On the other hand, geodetic data are not yet able to resolve any tectonic
302 deformation and thus to evaluate the loading rate of faults (Henrion et al., 2020). Even though the Drouet et al.
303 (2020) catalog, based on FCAT-17 catalog, is supposedly devoid of anthropic seismicity (Cara et al., 2015;
304 Manchuel et al., 2018), one can then ask whether the current seismicity is totally representative of the undergoing
305 long-term tectonic processes or presently modulated by surface loads such as the post-glacial rebound (e.g. Craig
306 et al., 2016), aquifer loads, erosion or incision (e.g. Bettinelli et al., 2008; Steer et al., 2014; Craig et al., 2017). If

307 so, the assumption that the main driver of seismicity is tectonic loading breaks down and our method used to assess
308 seismic hazard must be completed by physics-based constraints of such transient stress release (Calais et al., 2016).
309 Distinguishing seismic sources triggered by tectonic loading from other driven forces is an extremely difficult
310 task. The earthquake catalog contribution (Section 2.3) might then not be appropriate.

311 Additionally, the magnitudes of historical events from the FCAT-17 catalog (before the 1960s), and thus the ones
312 from Drouet et al. (2020), seem to be overestimated (or the instrumental events have underestimated magnitudes
313 even though it seems less probable) and a bias of the MFD is thus expected (Beauval and Bard, 2022; Doubre et
314 al., 2022). For the URG case, 3 bins out of 7 of the observed MFD are estimated from the instrumental period. The
315 bins estimated from the historical period have thus slightly more weight in the catalog constraint (Section 2.3).

316 We test an alternative constraint inferring that the possible magnitude and frequency of M_{max} must be consistent
317 with the observed largest event over the observation period (~ 146 yrs), meaning that it has to be larger than or
318 equal to the known largest event while the return period of the largest event cannot be significantly shorter than
319 the observation period (Approach 2 from Michel et al., 2018). This constraint is equivalent to considering that no
320 earthquakes with a magnitude greater than the largest event in the observation period occurred during the time
321 period covered by the observed catalog. Theoretically, this constraint imposes a lower bound on M_{max} and its
322 recurrence time. The results obtained using this constraint together with the moment budget and scaling law ones
323 are shown in Figure 7. Since M_{max} frequency differs for the tapered and truncated models, the new constraint
324 imposes different lower bounds for the two models. The truncated model rejects scenarios with M_{max} below $M_w 5.5$
325 more strongly. P_b is not constrained by the observed seismicity catalog but higher values of the b-value seem
326 slightly more probable (inset in Figure 7). The marginal probabilities $P(\tau | M_w = 5.9)$ and $P(\tau | M_w = 6.3)$ for
327 the tapered and truncated models have peaks at $\sim 12,500$ yrs and $\sim 63,000$ yrs, respectively.

328

329 **5.3 Strike slip component**

330 In this study, as well as in Chartier et al. (2017), we assume solely along-dip displacement since it is the only
331 published neo-tectonic information available. Nevertheless, recent paleo-seismological data on the Black Forest
332 fault near Karlsruhe (north of our study area) suggest 5.9 m of cumulative strike-slip, in contrast to 1.2 m of
333 cumulative vertical slip, over the last 5.9 kyrs (Pena-Castellnou et al., 2023). Those displacements seem to be
334 associated with at least three paleo-earthquakes. This suggests (1) that the Black Forest fault has been active during

335 the Quaternary period and that (2) strike-slip might be predominant. The ratio between strike- and dip-slip from
336 the Black Forest event would be then equal to 4.8. We thus test a scenario where the Black Forest fault is associated
337 with a maximum vertical slip deficit rate of 0.18 mm/yr, as proposed by Jomard et al. (2017), and where we
338 multiply the maximum slip deficit rate of all faults considered by 4.8. The results and the revised MDR for each
339 fault are shown in Figures 8 and S18. $P_{M_{max}}$ peaks at M_w 6.8 and M_w 6.6 for the tapered and truncated models,
340 respectively. They are associated with the marginal probabilities $P(\tau | M_w = 6.8)$ and $P(\tau | M_w = 6.6)$ that both
341 peak at ~16,000 yrs for the tapered and truncated models. Note that Pena-Castellnou et al. (2023) suggest that
342 earthquakes of potentially M_w 6.5 occurred north of our study area. P_b peaks at 0.7 for both the tapered and
343 truncated models, thus at lower values than taking into account the vertical-slip component alone.

344 The previous scenario tested (Figure 8) takes two more faults (i.e. Weinstetten and Lehen-Schonberg faults) into
345 account than in Chartier et al. (2017), as these two faults are not present within the BDFA (the French database of
346 potentially active faults; Jomard et al., 2017). The results obtained by selecting faults as defined by Chartier et al.
347 (2017) and applying the strike slip assumption are provided in Figure S19. $P_{M_{max}}$ peaks at M_w 6.7 and M_w 6.6 for
348 the tapered and truncated models, respectively, very similar to the scenario taking all four faults, as the moment
349 deficit rate is dominated by the Rhine River and Black Forest faults. Note that the marginal probabilities $P(\tau | M_w)$
350 and $P(\tau_{max} | M_{max})$ seem to get more noisy, likely due to the shape of the MDR PDF which skews heavily towards
351 zero (black line in Figure S18.e).

352 **5.4 Multi-segment rupture**

353 In this study we assume that all faults can rupture simultaneously. Nevertheless, the Black Forest Fault is initially
354 taken as inactive, and the traces of the Weinstetten and Lehen-Schonberg faults are separated by at least 7.9 km.
355 According to Wesnousky (2006), multi-segment ruptures are associated with low probability when the inter
356 segment distance exceeds 5 km. Consequently, the seismogenic potential scenario from Section 4 would be an
357 overestimation. On the other hand, according to Castellnou et al., 2022, the Black Forest Fault is in fact active and
358 seismogenic, and could be assumed to rupture with other faults. Additional structures might actually link all the
359 faults together (e.g. Lutz and Cleintuar, 1999; Bertrand et al., 2006; Rotstein and Schaming, 2011). In this case,
360 the seismogenic potential scenario from Section 4 would be interpreted as an underestimation.

361 Finally, we only consider the faults within a finite zone, which controls the total seismogenic area of the faults (i.e.
362 the moment-area scaling law effect), whereas the faults continue northwards and southwards to a lesser extent.

363 According to Weng and Yang (2017), the aspect ratio (width to length ratio of a rupture) of dip-slip events barely
364 reaches beyond 8. Taking a seismogenic width of 18 km (our maximum estimate), the maximum length of
365 earthquakes would then be 144 km, while the full length of the URG faults considered, including the Black Forest
366 fault, is ~250 km (~160 km if the Black Forest fault is not included). The rupture of all the faults would then be
367 unlikely. On the other hand, strike-slip events do not seem to be capped by any aspect ratio (Weng and Yang,
368 2017), so $M_w > 7.5$ events cannot be excluded in this context.

369 6 CONCLUSION

370 In this study, we investigate the seismogenic potential of the south-eastern URG, building on the work by Chartier
371 et al. (2017). Based on a complex fault network (Nivière et al., 2008), we evaluate scenarios that have not been
372 accounted for previously, exploring uncertainties on M_{max} , its recurrence time, the b -value, and the moment
373 released aseismically or through aftershocks (see Table 2 for a summary of the results considering the different
374 scenarios). Uncertainties for the MDR, the observed MFD, and the moment-area scaling law are also explored.
375 Given the four faults considered, and the scenario in which the Black Forest fault is no longer active but where the
376 other faults can still rupture simultaneously, the M_{max} maximum probability is estimated at $M_w 6.1$ and $M_w 5.8$
377 using the tapered or the truncated seismicity models respectively. Nevertheless, $P_{M_{max}}$ for the truncated model has
378 a second peak at $M_w 5.2$ and the recurrence time of events of such magnitude (not only M_{max}), $P(\tau | M_w = 5.2) \sim$
379 2,000 yrs, is much shorter than the one estimated using the main peak, $P(\tau | M_w = 5.8) \sim 10,000$ yrs. Again
380 considering the scenario excluding the Black Forest fault, there is a 99% probability that M_{max} is less than 7.3
381 using either the tapered or truncated models. In contrast, when strike-slip kinematics are considered as described
382 in Section 5.3 and the Black Forest Fault is taken into account, there is a 99% probability that M_{max} is less than
383 7.6 and 7.5 for the tapered and truncated models, respectively. This is our preferred scenario as it is based on recent
384 findings for strike-slip mechanisms, although the assumptions made in this analysis are debatable (i.e. strike-
385 slip/dip-slip ratio evaluated on a fault just north of our zone of study and applied to all faults; Section 5.3).
386 It should be noted that seismic hazard studies often place an upper bound on the values of M_{max} considered. In
387 the case of the URG, studies that use varying approaches to ours, have yielded values comparable to, or marginally
388 lower than the 99th percentile of $P_{M_{max}}$ of our strike-slip scenario (e.g. M7.4, M 7.1 and M7.5 for Grunthal et al.,
389 2018, Drouet et al., 2020, and Danciu et al., 2021, respectively).

390 In any case, within this study, strong assumptions still had to be made that certainly affected the results. It includes
391 the methodology used to decluster the earthquake catalogs, determining whether it is wise to compare the loading
392 rate of each fault with seismicity, opting to only consider the dip-slip component despite the fact that strike-slip is
393 highly probable, covering the possibility of multi-segment ruptures and even the choice of the faults to be
394 considered. Further work, from paleo-seismology, seismic reflection, geodesy, or earthquake relocation is needed
395 to obtain more information on the structures tectonically involved and their associated loading rates, and to better
396 constrain the URG seismic hazard.

397 **7 DATA AVAILABILITY**

398 The data used in this study are available via the publications mentioned in the main text.

399 **8 CODE AVAILABILITY**

400 The analyses reported in this paper were done using MATLAB.

401 **9 AUTHOR CONTRUBUTION**

402 SM, CD, LB and RJ conceptualized the study. SM performed the formal analysis with the help of JJ concerning
403 the declustering of the seismicity catalogs. SM prepared and wrote the manuscript with contributions from all co-
404 authors.

405 **10 COMPETING STATEMENT**

406 The authors acknowledge there are no conflicts of interest recorded.

407 **11 ACKNOWLEDGEMENT**

408 This study was supported by the LRC Yves Rocard (Laboratoire de Recherche Conventionnée CEA-ENS-
409 CNRS) and received funding from the European Research Council (ERC) under the European Union's Horizon
410 2020 research and innovation program (Geo-4D project, grant agreement 758210). RJ acknowledges funding
411 from the Institut Universitaire de France. The calculations were performed using MATLAB. We thank the
412 anonymous reviewers who helped us improve our study.

413

414 **12 REFERENCES**

- 415 Alwahedi, M. A., and Hawthorne, J. C.: Intermediate-Magnitude Postseismic Slip Follows Intermediate-
 416 Magnitude (M 4 to 5) Earthquakes in California, *Geophys. Res. Lett.*, 46, no. 7, 3676–3687,
 417 <https://doi.org/10.1029/2018GL081001>, 2019.
- 418 Anderson, J. G., and Luco, J. E.: Consequences of slip rate constraints on earthquake occurrence relations, *Bull.*
 419 *- Seismol. Soc. Am.*, 73, no. 2, 471–496, <https://doi.org/10.1785/BSSA0730020471>, 1983.
- 420 Avouac, J.-P.: From Geodetic Imaging of Seismic and Aseismic Fault Slip to Dynamic Modeling of the Seismic
 421 Cycle, *Annu. Rev. Earth Planet. Sci.*, 43, <https://doi.org/10.1146/annurev-earth-060614-105302>, 2015.
- 422 Baize, S., Cushing, E. M., Lemeille, F., and Jomard, H.: Updated seismotectonic zoning scheme of Metropolitan
 423 France, with reference to geologic and seismotectonic data, *Bull. la Société Géologique Fr.*, 184, no. 3,
 424 225–259, <https://doi.org/10.2113/gssgfbull.184.3.225>, 2013.
- 425 Barth, A., Ritter, J. R. R., and Wenzel, F.: Spatial variations of earthquake occurrence and coseismic
 426 deformation in the Upper Rhine Graben, Central Europe, *Tectonophysics*, 651–652, 172–185,
 427 <https://doi.org/10.1016/j.tecto.2015.04.004>, 2015.
- 428 Baumont, D., Manchuel, K., Traversa, P., Durouchoux, C., Nayman, E., and Ameri, G.: Intensity predictive
 429 attenuation models calibrated in Mw for metropolitan France, *Bull. Earthq. Eng.*, 16, no. 6, 2285–2310,
 430 <https://doi.org/10.1007/s10518-018-0344-6>, 2018.
- 431 Beauval, C., and Bard, P.: History of probabilistic seismic hazard assessment studies and seismic zonations in
 432 mainland France, *Comptes Rendus. Géoscience*, 353, no. S1, 413–440, <https://doi.org/10.5802/crgeos.95>,
 433 2022.
- 434 Bertrand, G., Elsass, P., Wirsing, G., and Luz, A.: Quaternary faulting in the Upper Rhine Graben revealed by
 435 high-resolution multi-channel reflection seismic, *Comptes Rendus Geosci.*, 338, no. 8, 574–580,
 436 <https://doi.org/10.1016/j.crte.2006.03.012>, 2006.
- 437 Bettinelli, P., Avouac, J.-P., Flouzat, M., Bollinger, L., Ramillien, G., Rajaure, S., and Sapkota, S.: Seasonal
 438 variations of seismicity and geodetic strain in the Himalaya induced by surface hydrology, *Earth Planet.*
 439 *Sci. Lett.*, 266, nos. 3–4, 332–344, <https://doi.org/10.1016/j.epsl.2007.11.021>, 2008.
- 440 Blanpied, M. L., Lockner, D. A., and Byerlee, J. D.: Frictional slip of granite at hydrothermal conditions, *J.*
 441 *Geophys. Res. Solid Earth*, 100, no. B7, 13045–13064, <https://doi.org/10.1029/95JB00862>, 1995.
- 442 Bommer, J. J., and Crowley, H.: The Purpose and Definition of the Minimum Magnitude Limit in PSHA
 443 Calculations, *Seismol. Res. Lett.*, 88, no. 4, 1097–1106, <https://doi.org/10.1785/0220170015>, 2017.
- 444 Bonjer, K.-P.: Seismicity pattern and style of seismic faulting at the eastern borderfault of the southern Rhine
 445 Graben, *Tectonophysics*, 275, nos. 1–3, 41–69, [https://doi.org/10.1016/S0040-1951\(97\)00015-2](https://doi.org/10.1016/S0040-1951(97)00015-2), 1997.
- 446 Calais, E., Camelbeeck, T., Stein, S., Liu, M., and Craig, T. J.: A new paradigm for large earthquakes in stable
 447 continental plate interiors, *Geophys. Res. Lett.*, 43, no. 20, 10,621–10,637,
 448 <https://doi.org/10.1002/2016GL070815>, 2016.
- 449 Cara, M. et al., SI-Hex: a new catalogue of instrumental seismicity for metropolitan France, *Bull. la Société*
 450 *Géologique Fr.*, 186, no. 1, 3–19, <https://doi.org/10.2113/gssgfbull.186.1.3>, 2015.
- 451 Carter, N. L., and Hansen, F. D.: Creep of rocksalt, *Tectonophysics*, 92, no. 4, 275–333,
 452 [https://doi.org/10.1016/0040-1951\(83\)90200-7](https://doi.org/10.1016/0040-1951(83)90200-7), 1983.
- 453 Chartier, T., Scotti, O., Clément, C., Jomard, H., and Baize, S.: Transposing an active fault database into a fault-
 454 based seismic hazard assessment for nuclear facilities – Part 2: Impact of fault parameter uncertainties on a
 455 site-specific PSHA exercise in the Upper Rhine Graben, eastern France, *Nat. Hazards Earth Syst. Sci.*, 17,
 456 no. 9, 1585–1593, <https://doi.org/10.5194/nhess-17-1585-2017>, 2017.
- 457 Churchill, R. M., Werner, M. J., Biggs, J., and Fagereng, Å.: Afterslip Moment Scaling and Variability From a
 458 Global Compilation of Estimates, *J. Geophys. Res. Solid Earth*, 127, no. 4,

- 459 <https://doi.org/10.1029/2021JB023897>, 2022.
- 460 Craig, T. J., Calais, E., Fleitout, L., Bollinger, L., and Scotti, O.: Evidence for the release of long-term tectonic
461 strain stored in continental interiors through intraplate earthquakes, *Geophys. Res. Lett.*, 43, no. 13, 6826–
462 6836, <https://doi.org/10.1002/2016GL069359>, 2016.
- 463 Craig, T. J., Chanard, K., and Calais, E.: Hydrologically-driven crustal stresses and seismicity in the New
464 Madrid Seismic Zone, *Nat. Commun.*, 8, no. 1, 2143, <https://doi.org/10.1038/s41467-017-01696-w>, 2017.
- 465 Danciu, L. et al.: The 2020 update of the European Seismic Hazard Model: Model Overview.
466 <https://doi.org/10.3929/ethz-b-000590386>, 2021.
- 467 Dieterich, J. H.: Modeling of Rock Friction Experimental Results and Constitutive Equations, *J. Geophys. Res.*,
468 84, no. B5, 2161–2168, <https://doi.org/10.1029/JB084iB05p02161>, 1979.
- 469 Doubre, C., Meghraoui, M., Masson, F., Lambotte, S., Jund, H., Bès de Berc, M., and Grunberg, M.:
470 Seismotectonics in Northeastern France and neighboring regions, *Comptes Rendus. Géoscience*, 353, no.
471 S1, 153–185, <https://doi.org/10.5802/crgeos.80>, 2022.
- 472 Drouet, S., Ameri, G., Le Dortz, K., Secanell, R., and Senfaute, G.: A probabilistic seismic hazard map for the
473 metropolitan France, *Bull. Earthq. Eng.*, 18, no. 5, 1865–1898, [https://doi.org/10.1007/s10518-020-00790-](https://doi.org/10.1007/s10518-020-00790-7)
474 7, 2020.
- 475 Fäh, D. et al.: The 1356 Basel earthquake: an interdisciplinary revision, *Geophys. J. Int.*, 178, no. 1, 351–374,
476 <https://doi.org/10.1111/j.1365-246X.2009.04130.x>, 2009.
- 477 Felzer, K. R.: Calculating California seismicity rates, Tech. Rep., Geological Survey (US),
478 <https://doi.org/10.3133/ofr20071437I>, 2008
- 479 Freymark, J., Sippel, J., Scheck-Wenderoth, M. Bär, K. Stiller, M. Fritsche, J.-G., and Kracht, M.: The deep
480 thermal field of the Upper Rhine Graben, *Tectonophysics*, 694, 114–129,
481 <https://doi.org/10.1016/j.tecto.2016.11.013>, 2017.
- 482 Fuhrmann, T., Caro Cuenca, M., Knöpfler, A., van Leijen, F. J., Mayer, M., Westerhaus, M., Hanssen, R. F., and
483 Heck, B.: Estimation of small surface displacements in the Upper Rhine Graben area from a combined
484 analysis of PS-InSAR, levelling and GNSS data, *Geophys. J. Int.*, 203, no. 1, 614–631,
485 <https://doi.org/10.1093/gji/ggv328>, 2015.
- 486 Grünthal, G., Stromeyer, D., Bosse, C., Cotton, F., and Bindi, D.: The probabilistic seismic hazard assessment of
487 Germany—version 2016, considering the range of epistemic uncertainties and aleatory variability, *Bull.*
488 *Earthq. Eng.*, 16, no. 10, 4339–4395, <https://doi.org/10.1007/s10518-018-0315-y>, 2018.
- 489 Guillou-Frottier, L., Carré, C., Bourguine, B., Bouchot, V., and Genter, A.: Structure of hydrothermal convection
490 in the Upper Rhine Graben as inferred from corrected temperature data and basin-scale numerical models,
491 *J. Volcanol. Geotherm. Res.*, 256, 29–49, <https://doi.org/10.1016/j.jvolgeores.2013.02.008>, 2013.
- 492 Heidbach, O. et al.: The World Stress Map database release 2016: Crustal stress pattern across scales,
493 *Tectonophysics*, 744, 484–498, <https://doi.org/10.1016/j.tecto.2018.07.007>, 2018.
- 494 Heidbach, O., Rajabi, M., Reiter, K., Ziegler, M. O., and WSM Team: World Stress Map Database Release
495 2016, V. 1.1. GFZ Data Services. <https://doi.org/10.5880/WSM.2016.001>, 2016.
- 496 Henrion, E., Masson, F., Doubre, C., Ulrich, P., and Meghraoui, M.: Present-day deformation in the Upper Rhine
497 Graben from GNSS data, *Geophys. J. Int.*, 223, no. 1, 599–611, <https://doi.org/10.1093/gji/ggaa320>, 2020.
- 498 Hinsken, S., Ustaszewski, K., and Wetzel, A.: Graben width controlling syn-rift sedimentation: the Palaeogene
499 southern Upper Rhine Graben as an example, *Int. J. Earth Sci.*, 96, no. 6, 979–1002,
500 <https://doi.org/10.1007/s00531-006-0162-y>, 2007.
- 501 Jomard, H., Cushing, E. M., Palumbo, L., Baize, S., David, C., and Chartier, T.: Transposing an active fault
502 database into a seismic hazard fault model for nuclear facilities – Part 1: Building a database of potentially
503 active faults (BDFa) for metropolitan France, *Nat. Hazards Earth Syst. Sci.*, 17, no. 9, 1573–1584,

- 504 <https://doi.org/10.5194/nhess-17-1573-2017>, 2017.
- 505 Kraft, T., and Deichmann, N.: High-precision relocation and focal mechanism of the injection-induced
506 seismicity at the Basel EGS, *Geothermics*, 52, 59–73, <https://doi.org/10.1016/j.geothermics.2014.05.014>,
507 2014.
- 508 Leonard, M.: Earthquake Fault Scaling: Self-Consistent Relating of Rupture Length, Width, Average
509 Displacement, and Moment Release, *Bull. Seismol. Soc. Am.*, 100, no. 5A, 1971–1988,
510 <https://doi.org/10.1785/0120090189>, 2010.
- 511 Lutz, M., and Cleintuar, M.: Geological results of a hydrocarbon exploration campaign in the southern Upper
512 Rhine Graben (Alsace Centrale, France), *Bull. für Angew. Geol.*, 4, 3–80,
513 <https://doi.org/http://doi.org/10.5169/seals-221515>, 1999.
- 514 Manchuel, K., Traversa, P., Baumont, D., Cara, M., Nayman, E., and Durouchoux, C.: The French seismic
515 CATalogue (FCAT-17), *Bull. Earthq. Eng.*, 16, no. 6, 2227–2251, <https://doi.org/10.1007/s10518-017-0236-1>, 2018.
- 517 Marsan, D., Bouchon, M., Gardonio, B., Perfettini, H., Socquet, A., and Enescu, B.: Change in seismicity along
518 the Japan trench, 1990-2011, and its relationship with seismic coupling, *J. Geophys. Res. Solid Earth*, 122,
519 no. 6, 4645–4659, <https://doi.org/10.1002/2016JB013715>, 2017.
- 520 Mayer-Rosa, D., and Cadiot, B.: A review of the 1356 Basel earthquake: Basic data, *Tectonophysics*, 53, nos. 3–
521 4, 325–333, [https://doi.org/10.1016/0040-1951\(79\)90077-5](https://doi.org/10.1016/0040-1951(79)90077-5), 1979.
- 522 Mazzotti, S. et al.: FMHex20: An earthquake focal mechanism database for seismotectonic analyses in
523 metropolitan France and bordering regions, *BSGF - Earth Sci. Bull.*, 192, 10,
524 <https://doi.org/10.1051/bsgf/2020049>, 2021.
- 525 Michel, S., Avouac, J.-P., Jolivet, R., and Wang, L.: Seismic and Aseismic Moment Budget and Implication for
526 the Seismic Potential of the Parkfield Segment of the San Andreas Fault, *Bull. Seismol. Soc. Am.*, 108, no.
527 1, 19–38, <https://doi.org/10.1785/0120160290>, 2018.
- 528 Michel, S., Jolivet, R., Rollins, C., Jara, J., and Dal Zilio, L.: Seismogenic Potential of the Main Himalayan
529 Thrust Constrained by Coupling Segmentation and Earthquake Scaling, *Geophys. Res. Lett.*, 48, no. 13, 1–
530 10, <https://doi.org/10.1029/2021GL093106>, 2021.
- 531 Molnar, P.: Earthquake Recurrence Intervals and Plate Tectonics, 115–133.
532 <https://doi.org/10.1785/BSSA0690010115>, 1979.
- 533 Nivière, B., Bruestle, A., Bertrand, G., Carretier, S., Behrmann, J., and Gourry, J.-C.: Active tectonics of the
534 southeastern Upper Rhine Graben, Freiburg area (Germany), *Quat. Sci. Rev.*, 27, nos. 5–6, 541–555,
535 <https://doi.org/10.1016/j.quascirev.2007.11.018>, 2008.
- 536 Oleskevich, D. A., Hyndman, R. D., and Wang, K.: The updip and downdip limits to great subduction
537 earthquakes: Thermal and structural models of Cascadia, south Alaska, SW Japan, and Chile, *J. Geophys.*
538 *Res. Solid Earth*, 104, no. B7, 14965–14991, <https://doi.org/10.1029/1999JB900060>, 1999.
- 539 Pena-Castellnou, S. et al., Surface rupturing earthquakes along the eastern Rhine Graben Boundary Fault near
540 Ettlingen-Oberweier (Germany), *Tectonophysics*, 869, 230114,
541 <https://doi.org/10.1016/j.tecto.2023.230114>, 2023.
- 542 Rollins, C., and Avouac, J.-P.: A Geodesy- and Seismicity-Based Local Earthquake Likelihood Model for
543 Central Los Angeles, *Geophys. Res. Lett.*, 46, no. 6, 3153–3162, <https://doi.org/10.1029/2018GL080868>,
544 2019.
- 545 Rotstein, Y., and Schaming, M.: The Upper Rhine Graben (URG) revisited: Miocene transtension and
546 transpression account for the observed first-order structures, *Tectonics*, 30, no. 3,
547 <https://doi.org/10.1029/2010TC002767>, 2011.
- 548 Rouland, D., Haessler, H., Bonjer, K. P., Gilg, B., Mayer-Rosa, D., and Pavoni, N.: The Sierentz Southern-
549 Rhinegraben Earthquake of July 15, 1980. Preliminary Results, in *Developments in Solid Earth*

550 *Geophysics*, 441–446, <https://doi.org/10.1016/B978-0-444-99662-6.50086-1>, 1983.

551 Ruina, A., 1983, Slip instability and state variable friction laws, *J. Geophys. Res. Solid Earth*, 88, no. B12,
552 10359–10370, <https://doi.org/10.1029/JB088iB12p10359>.

553 Steer, P., Simoes, M., Cattin, R., and Shyu, J. B. H.: Erosion influences the seismicity of active thrust faults, *Nat.*
554 *Commun.*, 5, no. 1, 5564, <https://doi.org/10.1038/ncomms6564>, 2014.

555 Stirling, M., Goded, T., Berryman, K., and Litchfield, N.: Selection of Earthquake Scaling Relationships for
556 Seismic-Hazard Analysis, *Bull. Seismol. Soc. Am.*, 103, no. 6, 2993–3011,
557 <https://doi.org/10.1785/0120130052>, 2013.

558 Stucchi, M. et al.: The SHARE European Earthquake Catalogue (SHEEC) 1000–1899, *J. Seismol.*, 17, no. 2,
559 523–544, <https://doi.org/10.1007/s10950-012-9335-2>, 2013.

560 Traversa, P., Baumont, D., Manchuel, K., Nayman, E., and Durouchoux, C.: Exploration tree approach to
561 estimate historical earthquakes Mw and depth, test cases from the French past seismicity, *Bull. Earthq.*
562 *Eng.*, 16, no. 6, 2169–2193, <https://doi.org/10.1007/s10518-017-0178-7>, 2018.

563 Wells, D. L., and Coppersmith, K. J.: New empirical relationships among magnitude, rupture length, rupture
564 width, rupture area, and surface displacement, *Bull. Seismol. Soc. Am.*, 84, no. 4, 974–1002, doi:
565 <https://doi.org/10.1785/BSSA0840040974>, 1994.

566 Weng, H., and Yang, H.: Seismogenic width controls aspect ratios of earthquake ruptures, *Geophys. Res. Lett.*,
567 44, no. 6, 2725–2732, <https://doi.org/10.1002/2016GL072168>, 2017.

568 Wesnousky, S. G., Predicting the endpoints of earthquake ruptures, *Nature*, 444, no. 7117, 358–360,
569 <https://doi.org/10.1038/nature05275>, 2006.

570 Woessner, J. et al.: The 2013 European Seismic Hazard Model: key components and results, *Bull. Earthq. Eng.*,
571 13, no. 12, 3553–3596, <https://doi.org/10.1007/s10518-015-9795-1>, 2015.

572 Zaliapin, I., and Ben-Zion, Y.: Earthquake clusters in southern California I: Identification and stability, *J.*
573 *Geophys. Res. Solid Earth*, 118, no. 6, 2847–2864, <https://doi.org/10.1002/jgrb.50179>, 2013.

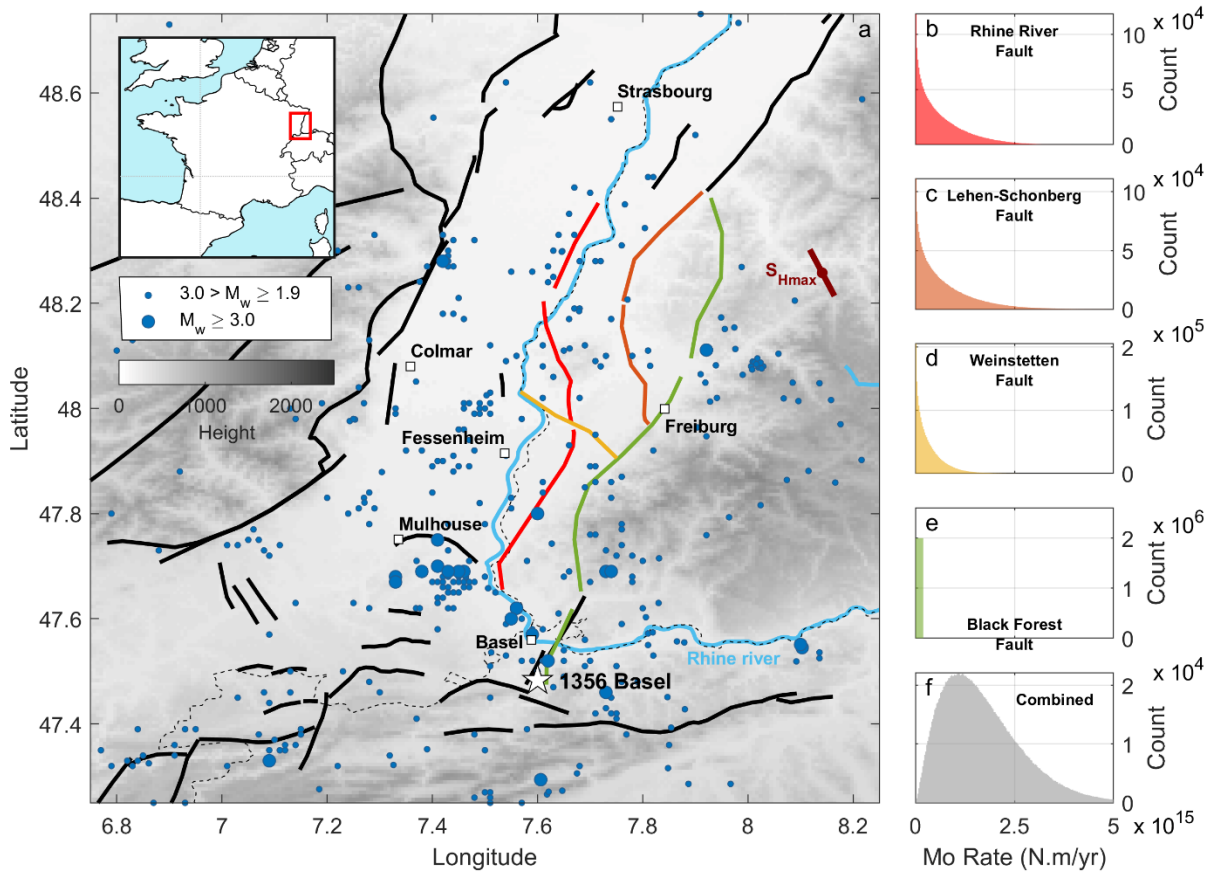
574

575

576

577

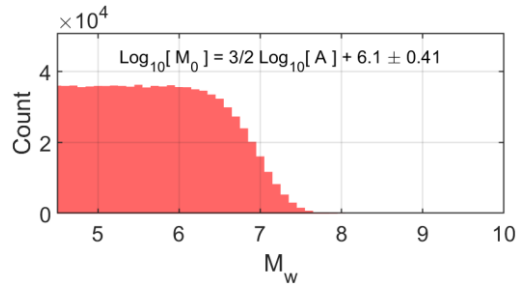
578



580

581 **Figure 1: (a) Regional setting and seismicity of the Upper Rhine Graben (Drouet et al., 2020). Black lines are faults**
 582 **while colored ones are the faults taken into account in this study. The fault network geometry is based on the BDFA**
 583 **database (Jomard et al., 2017) and Nivière et al. (2008). Blue dots are epicenters of $M_w > 2.2$ earthquakes since 1994.**
 584 **The white star indicates the 1356 Basel earthquake (magnitude ranging from $M6.5 \pm 0.5$ (Manchuel et al., 2017) to**
 585 **$M6.9 \pm 0.2$ (Fäh et al., 2009)). The brown bar indicates the approximate orientation of the maximum horizontal**
 586 **compressional stress (S_{Hmax}) (Heidbach et al., 2016, 2018). The thin dashed black line is the border between France**
 587 **and Germany. The nuclear powerplant of Fessenheim and the main cities are indicated by white squares. (b) to (f)**
 588 **Moment deficit rate PDFs (expressed in counts) for each of the four faults considered (colors are indicative of the faults**
 589 **in the left panel), and their combination (in grey).**

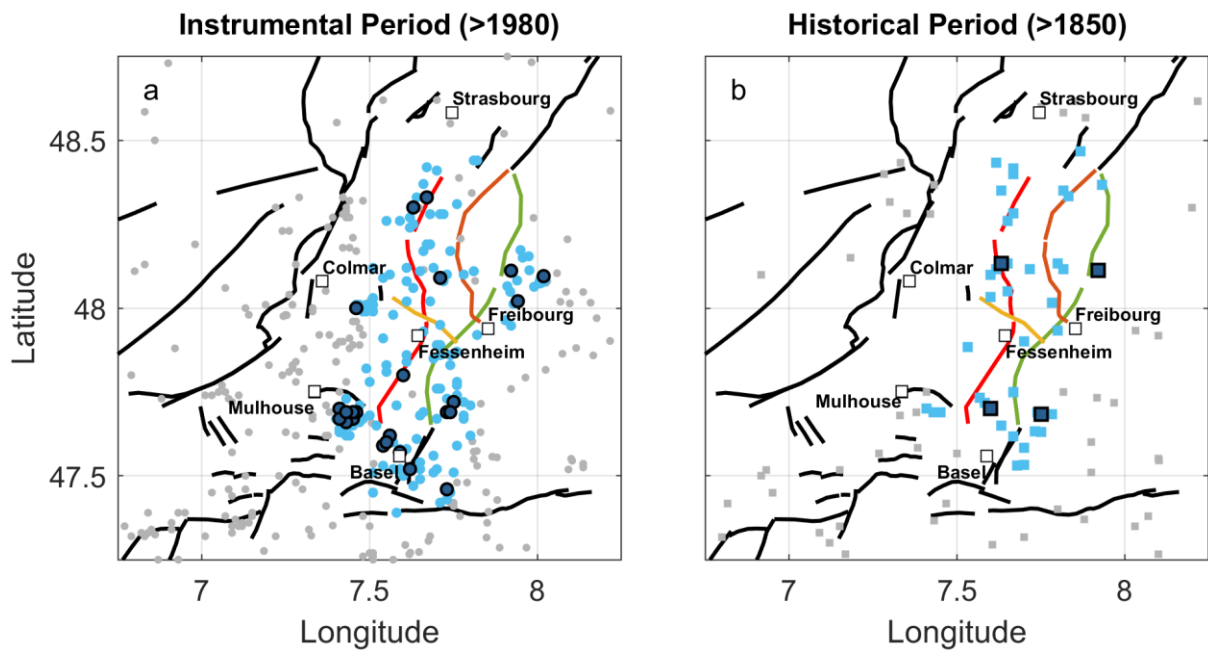
590



591

592 **Figure 2: PDF of M_w considering the along-dip moment-area scaling law of earthquakes from Leonard (2010). Note**
 593 **that the area from the Black Forest Fault is not included, as its loading rate is assumed equal to 0 mm/yr.**

594

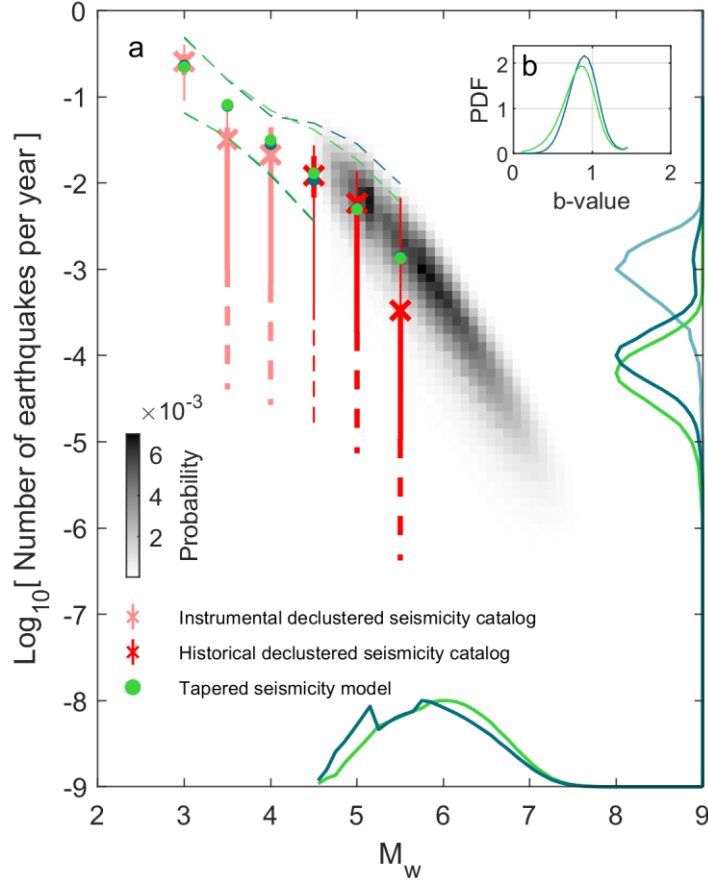


595

596 **Figure 3: Earthquake selection for the (a) instrumental (>1994) and (b) historical (>1850) periods. Gray dots and**
 597 **squares indicate all earthquakes with $M_c = 2.2$ and 3.2 for the instrumental and historical catalogs, respectively. Light**
 598 **blue dots and squares indicate earthquakes taken into account for the seismogenic potential analysis. Dark blue dots**
 599 **and squares indicate $M_w \geq 2.8$ and 4.3 earthquakes taken into account for the seismogenic potential analysis.**

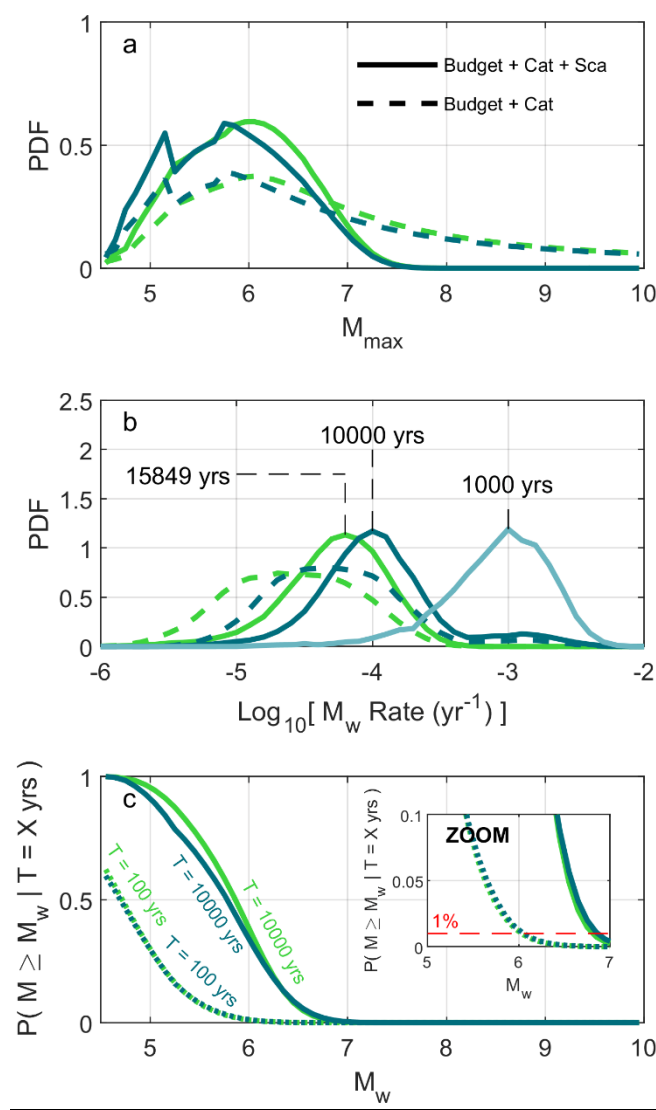
600

601



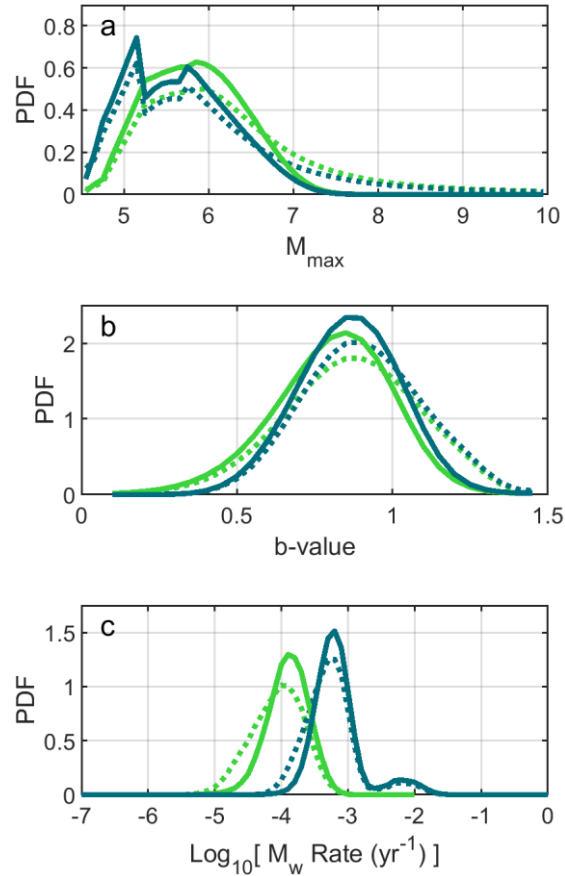
602

603 **Figure 4: (a) Seismogenic potential of the URG using all constraints: moment budget, observed magnitude-frequency**
 604 **distribution, and moment area scaling law. The rate of occurrence of historical and instrumental earthquakes, within**
 605 **their observation periods, are indicated by red and pink crosses and error bars, respectively. Thick and thin error bars**
 606 **indicate the 15.9-84.1% (1-sigma) and 2.3-97.7% (2-sigma) quantiles of the MFDs. Dashed lines show the spread of**
 607 **possible MFDs for the 2500 catalogs randomly generated to explore uncertainties. The green and blue colors are**
 608 **associated with the tapered and truncated long-term seismicity models. Green and blue dots show the means of the**
 609 **marginal PDF for the long-term seismicity. Dashed green and blue lines indicate the spread of the best 1% seismicity**
 610 **models. The marginal probabilities of M_{max} , $P_{M_{max}}$, are indicated by the solid lines on the M_w axis. They have been**
 611 **normalized so that their amplitude is equal to one instead of 0.60 and 0.59 for the tapered and truncated models,**
 612 **respectively. Green and dark blue lines on the earthquake frequency axis indicate the probability of the rate of events,**
 613 **τ , with magnitude $M_w = M_{Mode}$, thus $P(\tau | M_w = M_{Mode})$, with $M_{Mode}=6.1$ and 5.8 for the tapered and truncated**
 614 **models, respectively, considering all magnitudes in the seismicity models and not only the recurrence rate of M_{max} .**
 615 **They have also been normalized and their peaks were initially at 1.13 and 1.17 for the tapered and truncated models,**
 616 **respectively. The light blue line on the earthquake frequency axis indicates $P(\tau_{max} | M_{max} = 5.8)$ (for the truncated**
 617 **seismicity model only) and is normalized so that its amplitude equals one instead of 1.19. Note that the seismicity MFDs**
 618 **shown in the figure are not in the cumulative form. (b) Marginal probability of the b-value.**



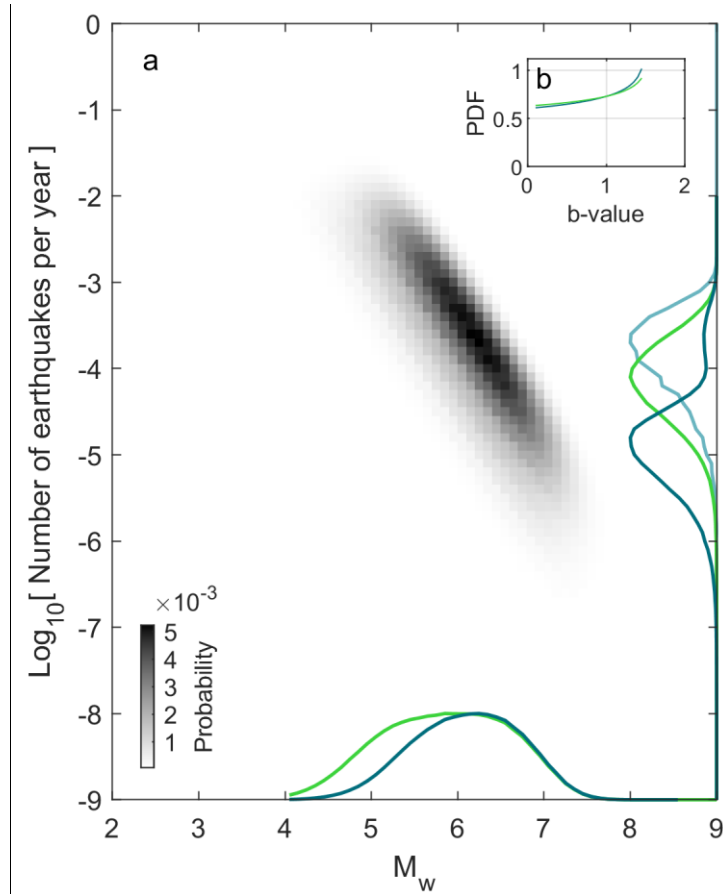
619

620 **Figure 5: (a) Evolution of the marginal PDF of M_{max} when adding the moment-area scaling law constraint. The green**
 621 **and blue colors in the figure are associated with the tapered and truncated long-term seismicity models. (b) Same as (a)**
 622 **but for the marginal PDF of the recurrence time of events: $P(\tau | M_w = 6.1)$ and $P(\tau | M_w = 5.8)$ for the tapered and**
 623 **truncated models (dark blue and green lines), respectively, and $P(\tau_{max} | M_{max} = 5.8)$ shown only for the truncated**
 624 **model (solid light blue line). (c) Probability of occurrence of earthquakes with a magnitude larger than M_w over a period**
 625 **of X yrs. We show the probability of occurrence of such events for the 100 yrs and 10,000 yrs time periods. In (a), (b)**
 626 **and (c), dotted lines represent the marginal PDFs considering both the moment budget and seismicity catalog constraint,**
 627 **the dashed lines indicate the PDFs when the earthquake scaling constraint is added. The inset in (c) is a zoom of the**
 628 **panel. The 1% probability of exceedance over a time period of 100 yrs is a typical order of magnitude for nuclear**
 629 **applications in France.**



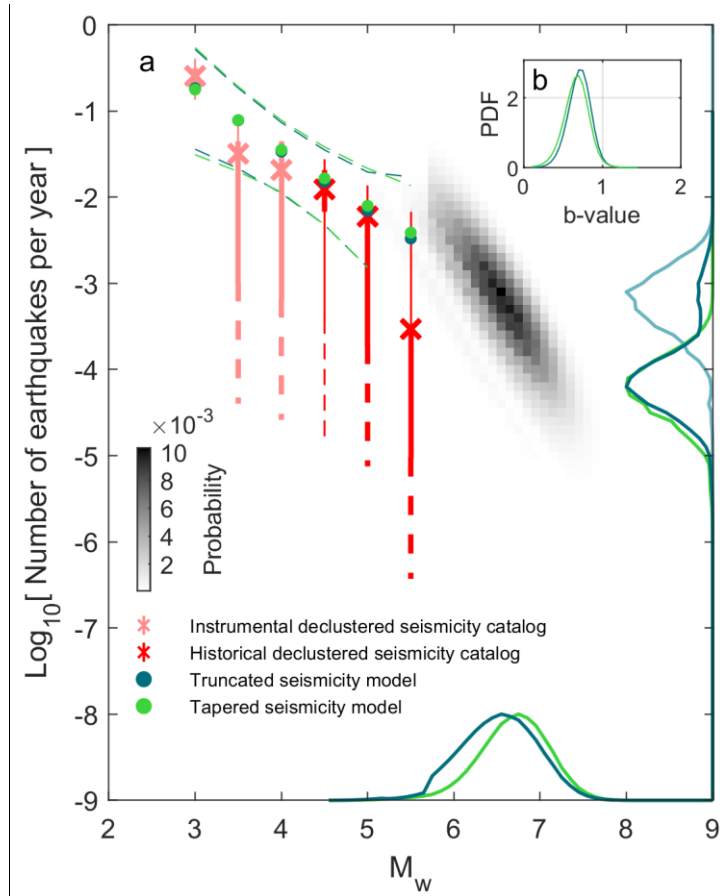
630

631 **Figure 6: Results using the declustering method from Zaliapin and Ben-Zion (2013) instead of Marsan et al. (2017)**
 632 **(Text S2). In this scenario, no probabilities of events to be mainshocks are defined. (a) M_{max} PDF. (b) b-value PDF. (c)**
 633 **$P(\tau | M_w = M_{Mode})$ PDF. Solid lines correspond to the results using all constraints while the dotted lines only use the**
 634 **moment budget and earthquake catalog constraints. Green and blue lines correspond to the tapered and truncated**
 635 **models, respectively. The results shown here are the ones taking a b-value equal to 1 for Zaliapin and Ben-Zion (2013)**
 636 **declustering method. The results for b-values of 0.5 and 1.5 are also shown in Figure S15 and are relatively similar to**
 637 **the ones obtained using a b-value of 1.0.**



638

639 **Figure 7:** Same as Figure 4 but only considering the constraints for the moment budget, the moment-area scaling law,
 640 and the one on M_{max} frequency considering the time period of the catalog (which serves as a lower bound constraint
 641 for M_{max} ; Section 5.2; Approach 2 from Michel et al., 2018). The marginal probabilities $P_{M_{max}}$ have been normalized so
 642 that their amplitude is equal to one instead of 0.46 and 0.58 for the tapered and truncated models, respectively. The
 643 same is true for $P(\tau | M_w = M_{Mode})$ which were initially of 0.85 and 0.81 of amplitude, and $P(\tau_{max} | M_{max} = 6.3)$ (for
 644 the truncated seismicity model only) which peaked at an amplitude of 0.85.



645

646 **Figure 8: Same as Figure 2 but considering a strike-slip slip rate component equivalent to 4.8 times the dip-slip estimate,**
 647 **and assuming the Black Forest Fault maximum long-term vertical slip rate is 0.18 mm/yr (as proposed by Jomard et**
 648 **al., 2017). Leonard et al.'s (2010) strike-slip moment-area scaling law is used here for the scaling law constraint, even**
 649 **though it is very similar to the dip-slip version. The marginal probabilities $P_{M_{max}}$ have been normalized so that their**
 650 **amplitude is equal to one instead of 1.02 and 0.88 for the tapered and truncated models respectively. The same is true**
 651 **for $P(\tau | M_w = M_{Mode})$ which were initially of 1.15 and 1.13 of amplitude, and $P(\tau_{max} | M_{max} = 6.6)$ (for the truncated**
 652 **seismicity model only) which peaked at an amplitude of 1.17.**

653

654 **Table 1: Fault parameters. \mathcal{U} and \mathcal{N} stands for uniform and normal distribution. The PDFs of each of these parameters**
 655 **and the resulting moment deficit rate for each fault are shown in Figure S3 to S6.**

Fault Name	Segment Name (from BDFA)	Dip (°)	Length (km)	Slip-Rate (mm/yr)	Seismogenic zone down-dip extent (km)	Evaporite layer thickness (km)
Rhine River Fault	FRR-1	$\mathcal{U}(50,80)$	$\mathcal{N}(35,2)$	$\mathcal{U}(0,0.07)$	(1) Uniform from 0 to 6 km in depth. (2) Linearly decreasing	$\mathcal{U}(0,2)$
	FRR-2	$\mathcal{U}(50,80)$	$\mathcal{N}(25,2)$			
	FRR-3	$\mathcal{U}(55,85)$	$\mathcal{N}(20,2)$			
Black Forest Fault	FFN-1	$\mathcal{U}(35,75)$	$\mathcal{N}(20,5)$	0	from 6 to 18 km depth.	
	FFN-2	$\mathcal{U}(40,80)$	$\mathcal{N}(50,2)$			
	FFN-3	$\mathcal{U}(35,75)$	$\mathcal{N}(35,2)$			
Lehen-Schonberg		$\mathcal{U}(40,80)$	$\mathcal{N}(54,2)$	$\mathcal{U}(0,0.1)$	Does not apply to the Black Forest Fault as its loading rate is assumed equal to 0 mm/yr	
Weinstetten		$\mathcal{U}(40,80)$	$\mathcal{N}(15,2)$	$\mathcal{U}(0,0.17)$		

656

657

658

Table 2: Summary of the results considering the different scenarios tested from section 4 to 5.3.

Scenarios	Modes of M_{max}	99% probability that M_{max} is below magnitude M_w	Mode of $P(\tau M_w = M_{Mode})$
Rhine River Fault + Lehen-Schonberg Fault + Weinstetten Fault <i>Dip-Slip Only</i> <i>Marsan et al. (2017) Declus.</i> (Section 4 / Fig. 4 and 5)	<u>Tapered Model</u> M_w 6.1 <u>Truncated Model</u> M_w 5.2 and 5.8	<u>Tapered Model</u> M_w 7.3 <u>Truncated Model</u> M_w 7.3	<u>Tapered Model</u> $\tau = 16,000$ yrs <u>Truncated Model</u> $\tau = 2,000$ and $10,000$ yrs
Rhine River Fault + Lehen-Schonberg Fault + Weinstetten Fault <i>Dip-Slip Only</i> <i>Zaliapin and Ben-Zion</i> <i>(2013) Declus.</i> (Section 5.1 / Fig. 6)	<u>Tapered Model</u> M_w 5.9 <u>Truncated Model</u> M_w 5.2 and 5.8	<u>Tapered Model</u> M_w 7.2 <u>Truncated Model</u> M_w 7.1	<u>Tapered Model</u> $\tau = 8,000$ yrs <u>Truncated Model</u> $\tau = 1,600$ and $8,000$ yrs
Rhine River Fault + Lehen-Schonberg Fault + Weinstetten Fault <i>Dip-Slip Only</i> <i>Marsan et al. (2017) Declus.</i> <i>Loose catalog constraint</i> <i>(Approach 2 from Michel et</i> <i>al., 2018)</i> (Section 5.2 / Fig. 7)	<u>Tapered Model</u> M_w 5.9 <u>Truncated Model</u> M_w 6.3	<u>Tapered Model</u> M_w 7.4 <u>Truncated Model</u> M_w 7.4	<u>Tapered Model</u> $\tau = 12,500$ yrs <u>Truncated Model</u> $\tau = 63,000$ yrs
Rhine River Fault + Lehen-Schonberg Fault + Weinstetten Fault + Black Forest Fault <i>Strike- and Dip-Slip</i> <i>Marsan et al. (2017) Declus.</i> (Section 5.3 / Fig. 8)	<u>Tapered Model</u> M_w 6.8 <u>Truncated Model</u> M_w 6.6	<u>Tapered Model</u> M_w 7.6 <u>Truncated Model</u> M_w 7.5	<u>Tapered Model</u> $\tau = 16,000$ yrs <u>Truncated Model</u> $\tau = 16,000$ yrs

660

661